

## Absolute cross section for $\text{Si}^{2+}(3s^2\ ^1S \rightarrow 3s3p\ ^1P)$ electron-impact excitation

D. B. Reisenfeld,\* L. D. Gardner, P. H. Janzen, D. W. Savin,<sup>†</sup> and J. L. Kohl  
*Harvard-Smithsonian Center for Astrophysics, Cambridge, Massachusetts 02138*

(Received 26 October 1998)

We have measured the absolute cross section for electron-impact excitation (EIE) of  $\text{Si}^{2+}(3s^2\ ^1S \rightarrow 3s3p\ ^1P)$  from energies below threshold to 11 eV above. A beams modulation technique with inclined electron and ion beams was used. Radiation at 120.7 nm from the excited ions was detected using an absolutely calibrated optical system. The fractional population of the  $\text{Si}^{2+}(3s3p\ ^3P^o)$  metastable state in the incident ion beam was determined to be  $0.210 \pm 0.018$  ( $1.65\sigma$ ). The data have been corrected for contributions to the signal from radiative decay following excitation from the metastable state to  $3s3p\ ^1P$  and  $3p^2\ ^3P$ , and excitation from the ground state to levels above the  $3s3p\ ^1P$  level. The experimental  $0.56 \pm 0.08$ -eV energy spread allowed us to resolve complex resonance structure throughout the studied energy range. At the reported  $\pm 14\%$  total experimental uncertainty level ( $1.65\sigma$ ), the measured structure and absolute scale of the cross section are in good agreement with 12-state close-coupling  $R$ -matrix calculations. [S1050-2947(99)06008-4]

PACS number(s): 34.80.Kw, 34.80.Dp

### I. INTRODUCTION

Over the past 25 years, electron-impact excitation (EIE) has been the subject of intense study, both experimentally and theoretically, as it is the dominant mechanism for the formation of emission lines in many laboratory and astrophysical plasmas. Absolute intensities of spectral lines excited by electron-impact excitation and their ratios can provide diagnostics of the temperature and density of an emitting plasma, and the abundances of the elements within the plasma [1,2]. In astrophysics, such emission lines have been observed through the use of ground-based observatories, and more recently, from space-based observatories to determine the physical conditions in myriad astrophysical sources ranging from the Sun to distant objects such as quasars and active galactic nuclei.

Modern space observatories such as the Hubble Space Telescope [3,4], the Solar Heliospheric Observatory [5], and the upcoming Chandra X-ray Observatory [6] measure UV and x-ray line intensities with detectors calibrated to a high degree of accuracy [7,8,6], placing more demand than ever on the atomic physics community to provide accurate atomic data. Theoretical calculations can provide the vast numbers of atomic rates used for the interpretation of emission line measurements, but experimental benchmark measurements are required to guide the development of the calculation methods [9,10].

To date, the great majority of experimental measurements of EIE have been for systems homologous with hydrogen (i.e., one electron outside a closed shell). Excitation in these systems is the most straightforward to calculate, as the cross section is dominated by direct excitation channels. However, many of the relevant ions for astrophysics, particularly ions used for density diagnostics, have EIE cross sections that are

dominated by autoionizing resonances [1]. Theoretical calculations for such ions are particularly difficult because the size of an individual resonance is extremely sensitive to the strength of the coupling to neighboring resonances [11].

Absolute measurements resolving resonance structure have been performed for the ions  $\text{Li}^+$ ,  $\text{Ti}^{20+}$ ,  $\text{Kr}^{6+}$ ,  $\text{Ar}^{6+}$ , and  $\text{Si}^{2+}$  [12–16]. In many cases, theory and experiment have disagreed. In the case of  $\text{Ti}^{20+}$ , theory and experiment were brought into agreement once the need to include radiative-damping channels was recognized in the theoretical formulation for EIE of highly charged ions [17]. In other cases, a satisfactory treatment is yet to be found. For  $\text{Kr}^{6+}$ , theory was brought into agreement with experiment only by arbitrarily positioning resonances on the energy scale [18]. For the  $3s^2\ ^1S \rightarrow 3s3p\ ^3P^o$  transition in  $\text{Ar}^{6+}$ , the measured strength of the large resonance at threshold was found to be higher by a factor of 2 than the theoretical prediction [15]. (Discussion of a previous  $\text{Si}^{2+}$  EIE measurement [16] is deferred to Sec. IV.) Evidently much more work is needed both theoretically and experimentally before the contribution of such complex structures to the excitation cross section can be understood.

Until recently, fluorescence yield measurements have been hampered by  $\leq 10^{-4}$  detection efficiencies and wide energy spreads. To overcome the low detection efficiency problem, Young [19] developed an optical system having an  $\approx 10^{-2}$  detection efficiency which was used to measure absolute  $\text{C}^{3+}(2s \rightarrow 2p)$  EIE and dielectronic recombination [20–22]. We have further refined the optical system, and have also improved the energy resolution of the apparatus by nearly threefold. These improvements have allowed us to use the fluorescence technique to measure the electron-impact excitation cross section for the  $3s^2\ ^1S \rightarrow 3s3p\ ^1P$  transition in  $\text{Si}^{2+}$ , and resolve its resonance structure. We are not aware of any other fluorescence technique measurements in a multiply-charged ion.

$\text{Si}^{2+}$  was chosen for study because of its astrophysical importance. The 120.7-nm emission line arising from the  $^1S \rightarrow ^1P$  excitation has been extensively observed in both solar and stellar plasmas [1,23,24]. Formed primarily at a

\*Present address: Los Alamos National Laboratory, M/S-D466, Los Alamos, NM 87545.

<sup>†</sup>Present address: Columbia Astrophysics Laboratory, Columbia University, New York, NY 10027.

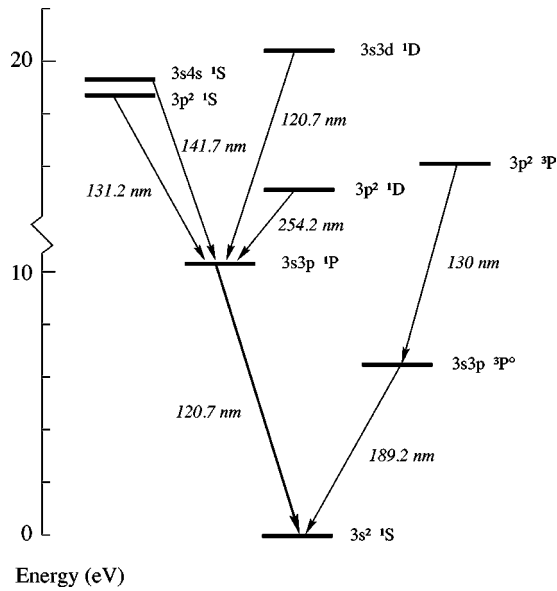


FIG. 1. Partial term diagram for  $\text{Si}^{2+}$ .

temperature of 60 000–80 000 K, the 120.7-nm line is a key diagnostic for the solar transition region [1]. It also has been observed recently in coronal mass ejections [25]. Excitations to and from the low-lying  $3s3p^3P^o$  metastable state give rise to many emission lines that, when measured in comparison to the 120.7-nm line, have made  $\text{Si}^{2+}$  an extensively utilized density diagnostic [26–28].

A partial energy-level diagram for  $\text{Si}^{2+}$  is given in Fig. 1. The  $3s^2^1S \rightarrow 3s3p^1P$  excitation cross section reported herein was measured by detecting radiation at 120.7 nm given off when ions excited by electron impact decay to the ground state. Because the  $\text{Si}^{2+}(3s3p^3P^o)$  metastable state is readily populated by the ion source, not all  $\text{Si}^{2+}$  ions are available to participate in excitation from the ground state. Additionally, excitation of metastable ions can lead to emission of photons in the bandpass of the optical system. To produce reliable excitation data, a careful analysis of the metastable beam content and its contribution to the detected signal has been performed.

## II. EXPERIMENTAL METHODS

### A. General

The experiment was performed by measuring the fluorescence yield of ions excited by electron impact. This technique has been used by this and other laboratories to measure a number of excitation cross sections [29–31,20]. In Ref. [20], our laboratory reported a measurement of  $\text{C}^{3+}$  EIE using an optical collection system having an efficiency of  $1 \times 10^{-2}$ . For the present work we have increased the detection efficiency by a factor of 2 by using a custom designed microchannel-plate (MCP) photodetector [32] rather than a commercial photomultiplier tube (PMT). Details of the experimental technique have been discussed in previous publications [33,34,20]. Presented here is a brief overview of the basic technique, followed by a more detailed description of recent improvements to the apparatus and of the methods used to overcome challenges specific to EIE measurements of  $\text{Si}^{2+}$ .

Ions are created in an electron cyclotron resonance (ECR) ion source, accelerated across a 10-kV potential, and charge to mass separated by a  $90^\circ$  deflection magnet to select  $\text{Si}^{2+}$  ions. The 20-keV  $\text{Si}^{2+}$  ions are then transported to a scattering chamber where the pressure is maintained at  $(2\text{--}3) \times 10^{-10}$  torr. Although the chamber has been subjected to hard bakeouts in the past, it was not baked for this experimental run. Immediately after entering the scattering chamber (see Fig. 2), the  $\text{Si}^{2+}$  ions pass through a final electrostatic charge-state preanalyzer which removes any  $\text{Si}^+$  and neutrals created by surface scattering or by charge transfer off residual background gas in the beam transport system. After exiting the preanalyzer, the ion beam travels 10 cm and crosses an electron beam inclined at an angle of nominally  $45^\circ$  relative to the ion beam. The beams' intersection volume is the region where EIE and other electron-ion collisions occur. A magnetic field of 10 G is applied coaxially with the electron beam to collimate it and increase its density. The electron beam is collected in a Faraday cup after it crosses the ion beam. The ion beam continues into an electrostatic charge-state post-analyzer, and its total current is measured with a Faraday cup or by using a Galileo 4039 channel electron multiplier (CEM) as a Faraday cup. A computer-

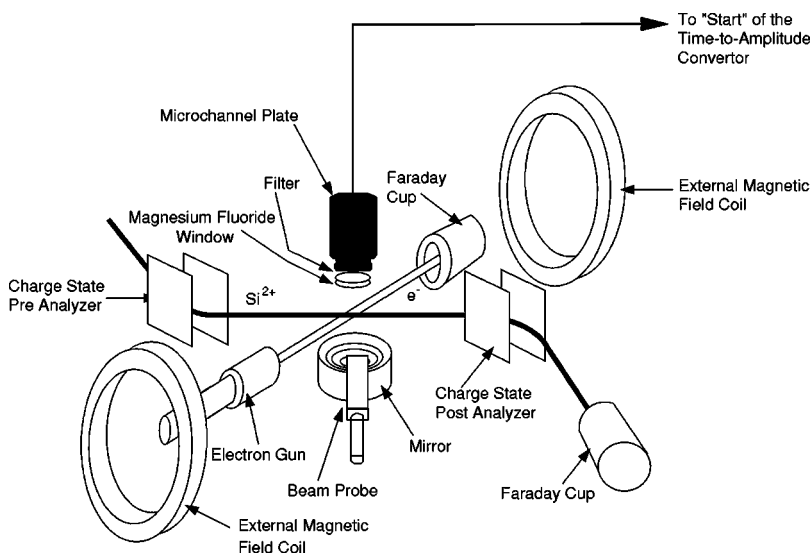


FIG. 2. Diagram of the experimental apparatus.

controlled beam probe is used to determine the spatial density profiles of each beam.

Below the beam intersection volume is a mirror which collects  $\pi$  steradians of the radiation emitted from the collision volume and concentrates it into the aperture of the MCP photodetector located above the collision volume. Some of the emitted photons are seen directly by the MCP, which subtends 0.32 sr. A  $\text{MgF}_2$  window isolates the scattering chamber from the MCP photodetector, which can be removed to perform optical alignments. The MCP face is coated with KBr, which was measured and found to increase the photoemission quantum efficiency (QE) at 120.7 nm from the bare-plate value of  $\sim 1\%$  to  $\sim 32\%$ . The achieved enhancement of the QE is comparable to the highest values reported in the literature [35,36]. The wavelength selectivity of the optical system is determined by the short-wavelength cutoff of the  $\text{MgF}_2$  window ( $\sim 110$  nm) and the long-wavelength cutoff of the KBr coating ( $\sim 160$  nm).

Two components, the ECR ion source and the MCP photodetector, represent significant upgrades of the instrument and warrant more detailed description. Over the past decade, ECR ion sources have almost become the standard for use in ion collision studies. These sources are noted for their ability to generate large currents of multiply charged ions, and to run continuously for weeks at a time with a high degree of stability [37–39]. The ion source used for this work is based on the design of a source constructed at the University of Giessen [40]. The source is notable in that it is powered by a 300-W 2.45-GHz magnetron (similar to that used in household microwave ovens); and in that the confinement field is provided solely by permanent magnets, thus providing a low-cost alternative to ECR ion sources operating at higher frequencies and employing electromagnets. Silane ( $\text{SiH}_4$ ) is used as the source gas for producing silicon ions, and the source is able to typically provide 30 nA of usable  $\text{Si}^{2+}$  ions on a continuous basis. Over a six month period of almost continuous operation, the source required no maintenance. This resulted in over a hundredfold increase in the effective data collection rate from previous experiment runs in which a Penning ion source was used.

A MCP photodetector was incorporated into the apparatus for two reasons. First, photodetectors utilizing MCP's usually have a higher detected-quantum efficiency (DQE) than their PMT counterparts [41,42]. The MCP photodetector constructed for the present work was measured to have a DQE at 121.6 nm of 21%, a factor of 2 higher than a typical commercially available PMT. Second, MCP operation is insensitive to magnetic fields of the strength used to collimate the electron beam [35,36]. Other UV photodetectors such as PMT's must be magnetically shielded to operate properly, as fields of only a few Gauss are sufficient to severely disturb the electrostatic focusing properties of a PMT's internal dynode chain [43]. We desire the photodetector to be as close as possible to the collision volume so as to have the largest possible acceptance angle. Magnetic shielding in close proximity to the collision volume would significantly disturb the magnetic-field homogeneity there, causing a spread in the trajectories of the individual electrons within the electron beam. This would in turn widen the distribution of collision angles between electrons and ions, broadening the energy distribution in the center-of-mass frame. Because a narrow

energy spread is required to resolve the resonance structure of the EIE cross section, the use of magnetic shielding is unacceptable. Using a MCP photodetector eliminates this concern.

Fluorescence detection measurement techniques determine the partial cross section for photon emission into a specific solid angle. The theoretically predicted partial EIE energy-averaged cross section,  $\langle d\sigma/d\Omega \rangle$ , for such fluorescence EIE experiments can be expressed as follows:

$$\left\langle \frac{d\sigma}{d\Omega}(E) \right\rangle = \int Y_{\Omega}(E', \theta_{z'}) \sigma(E') P(E, E') dE', \quad (1)$$

where the angular distribution of the emitted photons is taken into account by the factor  $Y_{\Omega}(E', \theta_{z'})$ ;  $E$  is the electron energy in the ion rest frame (which is essentially equivalent to the center-of-mass frame);  $\theta_{z'}$  is the angle the detected photon makes with respect to the electron-ion relative velocity vector which defines the  $z'$  axis;  $\sigma(E')$  is the theoretical total EIE cross section at energy  $E'$ ; and  $P(E, E')$  is the electron energy distribution function in the ion rest frame.

Integrating Eq. (1) over the solid angle collected by the experiment gives the predicted EIE energy-averaged cross section

$$\langle \sigma(E) \rangle = \int Y_{\Omega}(E') \sigma(E') P(E, E') dE', \quad (2)$$

where  $Y_{\Omega}(E')$  is the anisotropy factor averaged over the collected solid angle and for electric dipole transitions is given [44,45] by (dropping the prime notation from  $E$ )

$$Y_{\Omega}(E) = \frac{3(1 - \mathcal{P}(E) \langle \cos^2 \theta_{z'} \rangle_{\Omega})}{3 - \mathcal{P}(E)}. \quad (3)$$

Here  $\langle \cos^2 \theta_{z'} \rangle_{\Omega}$  is an average over the solid angle collected by the optical system, and  $\mathcal{P}(E)$  is the polarization of the emitted light as a function of electron energy. The polarization of the emitted radiation is customarily [44,46] defined as

$$\mathcal{P}(E) = \frac{I_{\parallel}(E) - I_{\perp}(E)}{I_{\parallel}(E) + I_{\perp}(E)}, \quad (4)$$

where  $I_{\parallel}(E)$  and  $I_{\perp}(E)$  are both measured at  $\theta_{z'} = 90^\circ$  and are, respectively, the intensities of emitted light polarized parallel to and perpendicular to the beams' relative velocity vector. For work in the vacuum UV, low signal rates and technical limitations often prevent an experimental determination of  $Y_{\Omega}(E)$ . In such cases theoretical calculations are sometimes used to specify  $Y_{\Omega}(E)$ . For the present work it was not possible experimentally to determine  $Y_{\Omega}(E)$ , but the large collecting solid angle of the optical system is expected to average out some of the anisotropy effects. The effects of polarization are discussed in more detail in Sec. III.

In the case where only one EIE transition contributes to the detected signal, the EIE energy-averaged cross section can be related to the experimentally determined parameters by

$$\langle \sigma \rangle = \frac{R_{\text{sig}}}{\xi \bar{v}_r} \frac{1}{\int N_I(\mathbf{x}) n_e(\mathbf{x}) \eta(\mathbf{x}, \tau) d^3 \mathbf{x}}. \quad (5)$$

Here  $R_{\text{sig}}$  is the EIE signal rate into the solid angle collected by the experiment;  $\xi$  is the fraction of the ion beam in the initial state of the excitation process under study (for  $\text{Si}^{2+}$ , either the  $3s^2 1S$  ground state or the  $3s3p^3 P^o$  metastable state);  $\bar{v}_r$  is the average relative velocity;  $N_I(\mathbf{x})$  and  $n_e(\mathbf{x})$ , respectively, are the particle densities of the ion and electron beams at a location in the intersection volume denoted by the spatial coordinate  $\mathbf{x}$ ; and  $\eta(\mathbf{x}, \tau)$  is the spatially varying detection efficiency of the optical system, where  $\tau$  is the lifetime of the excited state. The dependence of  $\eta(\mathbf{x}, \tau)$  on  $\tau$  accounts for the fact that an ion excited at location  $\mathbf{x}$  may radiate downstream of  $\mathbf{x}$  because of the finite lifetime of the excited state. If  $\tau$  is a significant fraction of the ion travel time through the region imaged by the optical system, the ion may radiate at a point where the detection efficiency is significantly different than it is at location  $\mathbf{x}$ .

For the present work, more than one excitation transition contributes to the detected signal. We define a new quantity related to Eq. (5) called the *weighted* cross section  $\langle \tilde{\sigma} \rangle$ , related to the experimentally determined parameters by

$$\langle \tilde{\sigma} \rangle = \frac{R_{\text{sig}}}{\bar{v}_r} \frac{1}{\int N_I(\mathbf{x}) n_e(\mathbf{x}) \eta(\mathbf{x}, \tau) d^3 \mathbf{x}}, \quad (6)$$

where  $R_{\text{sig}}$  now refers to the signal rate originating from all contributing EIE processes.  $N_I(\mathbf{x})$ ,  $n_e(\mathbf{x})$ , and  $\eta(\mathbf{x}, \tau)$  are defined as above, except that  $\eta$  is now the spatially varying detection efficiency for the dominant contributor to  $R_{\text{sig}}$  which, in this case, is the  $1S \rightarrow 1P$  transition.  $\langle \tilde{\sigma} \rangle$  is related to the cross section for the individual contributing processes by

$$\langle \tilde{\sigma} \rangle = \sum_i \xi_i \beta_i \langle \sigma_i \rangle. \quad (7)$$

Here  $\langle \sigma_i \rangle$  is the energy-averaged cross section for transition  $i$ ,  $\xi_i$  is the fraction of the beam in the initial state for transition  $i$ , and  $\beta_i$  is a scale factor to account for differences in detection efficiency,

$$\beta_i = \frac{\eta_i}{\eta}, \quad (8)$$

where  $\eta_i$  is the detection efficiency for transition  $i$ . Accounting for differences in detection efficiency through the use of the scale factor  $\beta_i$  is strictly valid only when the spatial dependences of  $\eta$  and  $\eta_i$  are identical. In practice, the difference in spatial dependence is sufficiently small that the use of a simple scale factor introduces a negligible error.

As we are interested in determining the measured cross section for the  $1S \rightarrow 1P$  transition, corrections must be made to  $\langle \tilde{\sigma} \rangle$  to remove the contributions from competing processes. The experimentally derived cross section for a specific transition  $j$  is related to  $\langle \tilde{\sigma} \rangle$  by

$$\langle \sigma_j \rangle = \frac{\langle \tilde{\sigma} \rangle - \sum_{i \neq j} \xi_i \beta_i \langle \sigma_i \rangle}{\xi_j \beta_j}. \quad (9)$$

The term  $\langle \tilde{\sigma} \rangle$  and the weighting factors  $\xi_i$  and  $\beta_i$  are pure experimental quantities.  $\langle \sigma_i \rangle$  can be determined either from theory or by independent experiments. A theoretical value for  $\langle \sigma_i \rangle$  can be used to determine  $\langle \sigma_j \rangle$  when the fractional contribution of  $\langle \sigma_i \rangle$  to  $\langle \tilde{\sigma} \rangle$  is sufficiently small that the associated uncertainty in  $\langle \sigma_j \rangle$  is negligible compared to the experimental uncertainties.  $\langle \sigma_i \rangle$  can be experimentally determined if there is some means of measuring the signal from transition  $i$  separately. This can be done for some transitions if, for example, filters are obtainable which can block radiation from all other transitions except that from transition  $i$ . For this work, both methods are used and will be further detailed in Sec. III.

### B. Determination of local particle densities

The local particle densities  $N_I(\mathbf{x})$  and  $n_e(\mathbf{x})$  are determined by scanning small Faraday cups across the electron and ion beams in the collision volume. The method is described in detail elsewhere [30,47]. Particle beam densities are derived by dividing the local current measurements by the area of the respective Faraday cup's circular aperture ( $\approx 0.25$ -mm diameter) and by the respective beam's velocity and charge. The total electron-beam current is determined by integrating the current density. The electron Faraday cup is biased positively to minimize secondary electron loss from the cup. The ion Faraday cup is biased for the same reason. However, secondary electrons liberated from the surface of the probe face by ion impact can be drawn through the Faraday cup aperture by the bias field. Thus the total integrated ion current cannot be used as an absolute current measurement. The total ion current is therefore determined from the current measured in the beam dump Faraday cup or in the CEM used as a Faraday cup. Typical ion beams have currents of 25–30 nA and a roughly circular cross sectional diameter of  $\approx 2$ -mm full width at half maximum (FWHM). Probes of the ion beam upstream and downstream of the optical center show that the beam is very well collimated. Typical electron beams have currents of 30  $\mu\text{A}$  and a roughly circular cross section of  $\approx 3$  mm diameter FWHM. Upstream and downstream probes of the electron beam show that at certain energies the beam has a slight divergence but is otherwise uniform. For the sake of efficiency the overlap integral [Eqs. (5) and (6)] is calculated assuming that the ion and electron beams are perfectly collimated. The divergence of the electron beam leads to at most a 3% error in the determination of the overlap integral.

### C. Determination of the optical detection efficiency

The optical detection efficiency  $\eta(x, y, z, \tau)$  can be written as

$$\eta(x, y, z, \tau) = T_{\text{win}} T_{\text{fil}} F_{\text{obs}} R_{\text{mir}} \frac{1}{\tau V} \int_z^\infty \exp\left[-\frac{z-z'}{\tau V}\right] \times Q(x, y, z') dz'. \quad (10)$$

TABLE I. Processes contributing to the measured signal. Energies are taken from Ref. [61], and lifetimes are taken from Refs. [48,49].

Excitation	Transition	Energy (eV)	$\xi_i\beta_i$	$\tau_i$ (ns)
$3s^2\ ^1S$	$\rightarrow 3s3p\ ^1P$	10.28	0.781	0.38
	$\rightarrow 3p^2\ ^1D$	15.15	0.095	110
	$\rightarrow 3p^2\ ^1S$	19.03	1.33	1.5
	$\rightarrow 3s4s\ ^1S$	19.72	1.40	4.9
	$\rightarrow 3s3d\ ^1D$	20.55	1.56	0.98
$3s3p\ ^3P^o$	$\rightarrow 3s3p\ ^1P$	3.72	0.209	0.38
	$\rightarrow 3p^2\ ^3P$	9.54	0.190	4.0

$T_{\text{win}}$  is the transmittance of the  $\text{MgF}_2$  window on the scattering chamber;  $T_{\text{fil}}$  is the transmittance of any filters used to narrow the bandpass;  $F_{\text{obs}}$  is the obscuration from the various baffles and screens in the optical system;  $R_{\text{mir}}$  is the reflectance of the mirror;  $v$  is the ion velocity; and  $Q(x,y,z')$  is the absolute photon detection efficiency for light emitted at  $(x,y,z')$ , where  $z'$  is now defined to lie along the ion-beam axis. The integral over  $z'$  accounts for the possibility that an ion may drift downstream in the ion beam before it radiatively decays. The optical elements are calibrated at multiple wavelengths. As indicated by Fig. 1, the possibility exists for the excitation of a number of levels giving rise to contributions to  $R_{\text{sig}}$  at not only 120.7 nm, but also at 189.2, 131.2, and 141.7 nm, and from a multiplet radiating near 130 nm. To cover this range, transmittance, reflectances, and detection efficiencies were measured at 119.9, 121.6, 130.5, and 189.8 nm for all optical elements individually. These wavelengths correspond to bright line-radiation sources readily generated by the gas-discharge lamp used for calibrations. The obscuration from the baffles and screens was determined from the measured geometry. The ion-beam velocity was derived from the ion source extraction potential. Calculated values of  $\tau$  [48,49] are given in Table I for the transitions considered in the present work. Excitations to some of the high-lying states decay via cascade to the ground state. For these, total cascade lifetimes are given.

$Q(x,y,z')$ , the spatially varying photon detection efficiency, was calculated with a fully three-dimensional ray-tracing code. This code takes into account the experimentally determined imaging properties of the mirror, the component of light emitted directly onto the MCP, any measured asymmetry in the location of baffles and apertures, and multiple reflections between any partially reflective elements. The code also takes into account the contribution to  $Q(x,y,z')$  from the experimentally determined variation of the MCP photodetector DQE as a function of the incidence angle of photons to the front MCP surface. Photons which strike within the channels of the MCP have a much lower probability of detection than photons striking the MCP webbing. As the channels are biased  $13^\circ$  to the plate normal, this leads to an asymmetric angular DQE dependence. The variation in the DQE of the MCP photodetector was therefore carefully mapped as a function of angle. The absolute DQE was determined by comparing the MCP to a CsTe photodiode calibrated by the National Institute of Standards and Technology (NIST).

#### D. Determination of ion-beam state populations

The parameter  $\xi$  takes into account the charge purity and the metastable content of the ion beam. The beam-steering apparatus purifies the beam so that only particles of  $m/q = 14$  propagate to the interaction chamber. Therefore,  $\text{N}^+$  is expected to be the only significant contaminant of the ion beam. Two methods were used to determine the level of nitrogen contamination. The first method takes advantage of the two isotopes of silicon,  $^{28}\text{Si}$  and  $^{29}\text{Si}$ , that have sufficient natural abundance to give rise to measurable beam currents of each. By comparing the natural abundance ratio (92.2:4.7) [50] to the ratio measured in the beam currents, one can hope to determine the degree of contamination. Ideally, we wish to compare the ratio of  $^{28}\text{Si}^{2+}$  to  $^{29}\text{Si}^{2+}$ , but this is complicated by the presence of significant quantities of  $^{28}\text{SiH}^{2+}$  ions which mask the  $^{29}\text{Si}^{2+}$  ions. However, we can make an appropriate comparison for  $\text{Si}^{4+}$  ions (which are aliased by  $\text{N}^{2+}$ ). The ratio of  $^{28}\text{Si}^{4+} + \text{N}^{2+}$  current to  $^{29}\text{Si}^{4+}$  current was 1.5: 0.073 nA, which allows us to set an upper limit of 0.06 nA on the  $\text{N}^{2+}$  content. When running pure nitrogen, the source typically produces  $\text{N}^+$  vs  $\text{N}^{2+}$  in the ratio 10:1 or less, from which we can argue for an upper limit on  $\text{N}^+$  contamination of 0.6 nA, or  $\sim 2\%$  of the typical total  $m/q = 14$  beam current (30 nA). Because it is possible that  $\text{N}^{2+}$  and  $\text{N}^+$  will not be produced in the same ratio when the principal gas is not nitrogen, we performed additional tests with a variety of gases not having ions that alias  $\text{N}^+$ , and measured the  $\text{N}^+$  yield. Care was taken to ensure that the gas delivery system was in an identical state as when running silane. From these tests, we observed  $\text{N}^+$  yields ranging from  $\approx 0$  to 0.75 nA. Based on these results, we set the level of  $\text{N}^+$  contamination fraction at  $0.01 \pm 0.01$ .

Beyond the issue of beam species purity, we expect that  $\xi$  will differ significantly from 1.0 because of the existence of the  $\text{Si}^{2+}(3s3p\ ^3P^o)$  low-lying metastable state. Ion sources are known to populate metastable levels readily [33,51,52], and if the lifetime of such a level is comparable to the ion travel time to the collision region, a significant metastable population will be present in the interaction region. Of the three  $J$  sublevels of  $\text{Si}^{2+}(3s3p\ ^3P^o)$ , the  $J=1$  level has the shortest lifetime (60  $\mu\text{s}$ ) [53,54]. This is much longer than the  $\sim 10\text{-}\mu\text{s}$  flight time from the ion source. The  $J=2$  level has a lifetime on the order of 1 min, and the  $J=0$  lifetime is longer still, as it must undergo a strongly forbidden 0-0 transition to decay [55].

We have studied the metastable state population in detail using two methods: the *fluorescence method* and the *beam attenuation method*. The beam attenuation method [56,52,57] involves filling a section of the beamline with gas that attenuates the ion beam, and measuring the transmitted ion beam current as a function of gas pressure. The metastable state will usually have a significantly higher charge exchange cross section than the ground state. Thus one will observe an initial steep drop in (log) transmitted current versus pressure corresponding to attenuation of both states, followed by a more gradual drop at higher pressure due to attenuation of the remaining ground-state beam. Extrapolation of the high-pressure (ground-state attenuation) slope to zero gas pressure yields the metastable fraction of the beam (see Fig. 3). We applied this technique by using both  $\text{H}_2$  and Ar as attenua-

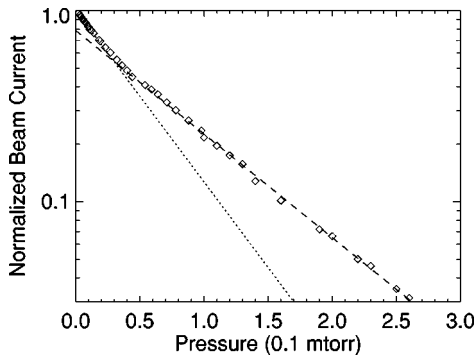


FIG. 3. Transmitted  $\text{Si}^{2+}$  ion current vs  $\text{H}_2$  ion gauge pressure. The dotted curve is a fit to the initially steep portion of the attenuation curve, corresponding to attenuation of both ground-state and metastable  $\text{Si}^{2+}$ . The dashed curve is a fit to the high-pressure portion of the curve, corresponding to attenuation of the remaining ground-state  $\text{Si}^{2+}$ . Extrapolation of the high-pressure slope to zero gas pressure yields the metastable fraction of the beam. The metastable fraction determined using this procedure is  $0.224 \pm 0.025$ . Use of the fluorescence method (see text) yields a metastable fraction of  $0.195 \pm 0.025$ . As neither method is necessarily superior to the other, the value adopted for this work is the average of the two,  $0.210 \pm 0.018$ .

tion gases, and determined a metastable fraction of  $0.224 \pm 0.025$ , where the uncertainty results primarily from scatter in the measured slopes among the different runs.

The fluorescence method, originally proposed by Lafyatis and Kohl [33], makes use of the radiation emitted by decay of the metastable state. We observed the absolute intensity of 189.2-nm light radiated as metastable  $\text{Si}^{2+}$  ions traverse the region imaged by the optical system. A PMT (Thorne EMI 9413) operating in the pulse counting mode was calibrated for this wavelength by comparing it to a photodiode calibrated by NIST. Using a variant of the raytrace code used to determine the detection efficiency for EIE runs, we determined the absolute number of 189.2-nm photons being emitted by ions in the beam. To determine the metastable fraction from the number of photons observed radiating (per unit length), it is necessary to know the lifetime of the metastable state. The  $J=1$  level has a measured lifetime of  $59.9 \pm 3.6 \mu\text{s}$  [53], which is in excellent agreement with recent sophisticated quantal calculations [54]. Because the lifetimes of the  $J=2$  and 0 levels are so much longer than that of the  $J=1$  level, essentially all of the radiation comes from the  $J=1$  level. Therefore, we are in fact determining the population solely of the  $J=1$  state. We can estimate the total metastable population by specifying how the metastable ions are distributed among the fine-structure levels. In the present case, it is likely that the electron density and temperature in the ion source are sufficiently high that the metastable levels should be equilibrated to their statistical population. (We then account for the slight depopulation of the  $J=1$  state after traveling the  $\sim 10 \mu\text{s}$  to the collision chamber.) By use of this method, we arrived at a total metastable fraction of  $0.195 \pm 0.025$ . The quoted uncertainties reflect the statistical uncertainty in the photon rate and the uncertainties in the lifetime measurement and radiometric calibration. Neither the fluorescence technique nor the beam attenuation technique is necessarily superior to the other; thus the value

TABLE II. Typical operating conditions.

$\text{Si}^{2+}$ current	30 nA
Electron current	30 $\mu\text{A}$
Photon backgrounds	
from electrons	200 $\text{s}^{-1}$
from $\text{Si}^{2+}$	80 $\text{s}^{-1}$
dark rate	3 $\text{s}^{-1}$
EIE signal rate	18 $\text{s}^{-1}$
Chopping pattern frequency	16.7 kHz
Pressure (ionization gauge reading)	$2 \times 10^{-10}$ torr

adopted in this work for the total metastable fraction is  $0.210 \pm 0.018$ .

### E. Determination of the EIE event rate

The measured EIE signal  $R_{\text{sig}}$  was determined using beam chopping and synchronous detection techniques which have been discussed in detail elsewhere [30,58–60]. For the present measurement the beam chopping pattern was as follows: (1) electrons and ions turned off, (2) electrons and ions turned on, (3) ions only turned on, and (4) electrons only turned on. The total chopping pattern was modulated at a frequency of 16.7 kHz to minimize any effects the modulation of the beams might have on the background gas in the collision chamber, and thus on the measured EIE signal [58,47]. Photons were detected in delayed coincidence with an electronic pulse which signaled the end of the data-acquisition chopping pattern. The photons provided the “start” pulse for a time-to-amplitude converter and the electronic pulse provided the “stop” pulse. Table II lists the experimental operating conditions for a typical data run.

The EIE data were collected over the course of three months. During EIE data collection, the electron beam was switched between two energies with a typical period of 50 s. In this way data were collected, nearly simultaneously, at two energies  $\leq 1$  eV apart, which allowed each set of measurements to be referenced to another measurement. This energy-switching technique allowed the stability over time of the apparatus to be monitored. Also, data points taken early in the course of the experimental run were retaken at the end as an additional check on stability. All data taken at the same energies agreed within statistical error, regardless of when they were taken, confirming the long-term stability of the detection apparatus.

### F. Uncertainties

Experimental uncertainties fall into two categories: relative uncertainties which vary from point to point, and systematic uncertainties which do not affect the shape of the data but only the overall scale. The relative uncertainties are dominated by counting statistics, but also include run-to-run variations in the overlap integral arising from minor shifts in beam densities and positions. Total relative uncertainties, reported at the 90% confidence limit ( $1.65\sigma$ ), are typically  $\sim 5\%$  of the above-threshold cross section.

A summary of the known sources of systematic uncertainty for the present measurement, reported at the same (90%) confidence limit, is given in Table III. The single

TABLE III. Summary of uncertainties. All uncertainties are quoted at a confidence level considered to be equivalent to a statistical 90% confidence level.

Sources of uncertainty	Uncertainty
Uncertainty in beam densities	
ion beam current measurement	5%
current measurement in electron beam Faraday cup	1%
electron beam probe biasing procedure	5%
correction factor for N <sup>+</sup> contamination	1%
uncertainty in ground state population due to metastable state	3%
Uncertainties in beams' geometric-overlap/detection-efficiency factor	
spatial coordinates of the collision volume	3%
computational error in the overlap determination	1%
assumption that electron beam is perfectly collimated	3%
radiometric calibration	
NIST standard photodiode accuracy	8%
photodiode calibration variation	1%
MCP angular variation map	1%
calibration of filters used in MCP calibration	2%
variation in MCP QE	2%
mirror reflectance	3%
MgF <sub>2</sub> window transmittance	2%
computational error in raytracing program	1%
Uncertainty due to excitation from metastable state	3%
Total quadrature sum <sup>a</sup>	13%

<sup>a</sup>Total experimental uncertainty (in %) is equal to  $[13^2 + (90\% \text{ statistical uncertainty})^2]^{1/2}$ .

largest uncertainty in the EIE measurement arises from the NIST photodiode calibration ( $\pm 8\%$ ) to which the MCP photodetector is compared. The photodiode was calibrated by NIST before and after the MCP calibration. The photodiode efficiency was shown to have dropped by  $\sim 2\%$ . The MCP DQE was measured before and after the experimental run, and the efficiency at 120.7 nm was found to have dropped by 4%. Average numbers for both the photodiode and the MCP efficiencies are incorporated into the data analysis. The uncertainty associated with the drop in efficiencies is taken to be half of the percentage drop. Great care was taken in the radiometric calibrations of other elements in the optical system to assure that they introduce only small additions to the total experimental uncertainty. An error of 3% is introduced into the determination of the overlap integral by the uncertainty in the location of the beams' intersection volume in the object space of the optical system.

All of the experimental uncertainties listed in Table III are treated as independent, and are added in quadrature to yield a  $\pm 13\%$  absolute uncertainty in the experimental scale. The total uncertainty for each EIE data point is given by adding in quadrature the relative uncertainty for that data point with the absolute scale uncertainty of the experiment.

### III. ANALYSIS AND RESULTS

Our measurement of the weighted EIE cross section  $\langle \tilde{\sigma} \rangle$  is presented in Fig. 4. The data points (open circles) were determined from the measured values of  $R_{\text{sig}}$  as defined by Eq. (6). Data were collected across a range of collision energies from 8.5 to 21.5 eV. The heavy error bars in Fig. 4

represent the relative uncertainty at the 90% confidence level ( $1.65\sigma$ ). The total (systematic plus relative) experimental uncertainty ( $\pm 14\%$ ) is shown by the thin error bars on the 10.8- and 17.2-eV data points. Excitation of the  $^1S \rightarrow ^1P$  transition is the dominant but not sole contributor to  $R_{\text{sig}}$ . Some fraction of  $R_{\text{sig}}$  results from excitation from the metastable  $3s3p\ ^3P^o$  state to either the  $3s3p\ ^1P$  level, which has a threshold of 3.72 eV (leading to a nonzero signal below the  $^1S \rightarrow ^1P$  threshold), or to higher states which then cascade. In addition, above an energy of 15.15 eV, excitation from the  $^1S$  ground state to higher states gives off photons within the bandpass of the optical system via cascades. Table I lists all EIE transitions expected to contribute significantly to  $R_{\text{sig}}$ , and their threshold energies [61]. Other transitions are energetically possible, but have not been included because they are expected either to have negligible cross sections, or to have cascade times sufficiently long that the excited ions will have traveled beyond the field of view of the optical system before they radiate.

The EIE cross sections for all of the transitions in Table I were calculated by Griffin, Pindzola, and Badnell [48], using a 12-state close-coupling (12CC)  $R$ -matrix calculation method. Apart from the primary  $^1S \rightarrow ^1P$  transition, theory indicates these transitions are expected to make small contributions to  $R_{\text{sig}}$  across most of the covered energy range. The single largest contributor is the  $^3P^o \rightarrow ^3P$  transition, which is expected to account for  $\sim 10\%$  of the signal above the  $^1S \rightarrow ^1P$  threshold.

The heavy curve in Fig. 4 represents the theoretical value of  $\langle \tilde{\sigma} \rangle$  incorporating the theory of Ref. [48] and the mea-

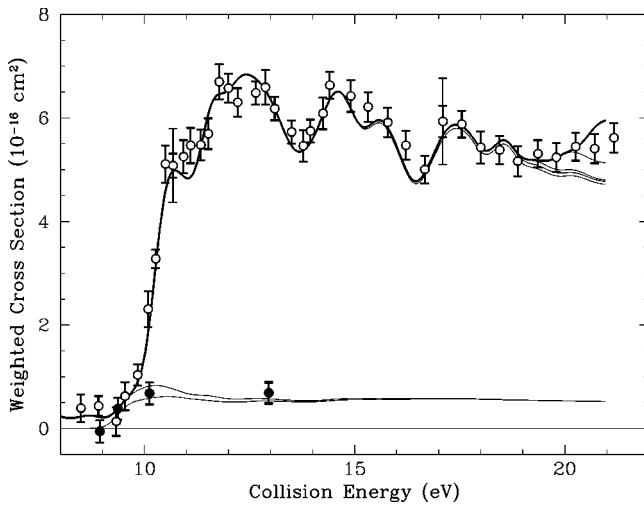


FIG. 4. Measured energy-averaged EIE cross section  $\langle \tilde{\sigma} \rangle$  for  $\text{Si}^{2+}$  which, in addition to  $3s^2 1S \rightarrow 3s3p^1P$  excitation, includes weighted contributions from cascades from higher levels and from excitation of the metastable  $3p^2 3P$  level. The data (open circles) were determined from the measured values of the event rate  $R_{\text{sig}}$ . The heavy error bars represent the relative uncertainty at the 90% confidence level, and the thin error bars on the 10.8- and 17.2-eV data points represent the total experimental uncertainty. The heavy curve represents the theoretical value of  $\langle \tilde{\sigma} \rangle$  incorporating the theory of Ref. [48], and the measured detection efficiencies and population fractions (used to determine the weighting for the theoretical contributions). The thin curves show the cumulative buildup of contributions to  $\langle \tilde{\sigma} \rangle$  from each term  $\xi_i \beta_i \langle \sigma_i \rangle$  of Eq. (7). Data were also collected (solid circles) with a CaF cutoff filter in place, isolating the  $3p^2 3P$  multiplet radiation near 130 nm. These data are scaled by a factor  $\xi_i \beta_i = 0.190$  to indicate the contribution of  $3p^2 3P - 3s3p^3P^o$  radiation to  $\langle \tilde{\sigma} \rangle$ , and are to be compared to the lowest curve.

sured detection efficiencies and population fractions. The thin curves show the cumulative buildup of contributions to  $\langle \tilde{\sigma} \rangle$  from each term  $\xi_i \beta_i \langle \sigma_i \rangle$  of Eq. (7). The cross sections  $\langle \sigma_i \rangle$  are determined by convolving the theoretical cross section with a Gaussian having a FWHM of 0.56 eV, representing the energy resolution of the experiment. The factor  $\xi_i$  is taken to be the ground-state population of the ion beam for transitions out of the ground state, and the metastable population for transitions out of the metastable state. The scale factor  $\beta_i$  takes into account differences in detection efficiency. For example, after being excited from the ground state, the  $3s4s^1S$  level radiates to  $3s3p^1P$  at 131.2 nm, which then radiates to the ground state at 120.7 nm. The total cascade lifetime is 4.9 ns [48], which is not quite rapid enough for all  $3s4s^1S$  excitation to radiate within the optical system; only 91.8% of the excited ions radiate in time to be detected. The detection efficiency of the optical system for 131.2-nm radiation is 95.1% of the efficiency for 120.7-nm radiation. The population fraction  $\xi_i$  is the ground-state population fraction of 0.781.  $\xi_i \beta_i$  for this contribution is therefore  $0.781 \times 0.918 \times (0.951 + 1.00) = 1.40$ . Values for  $\xi_i \beta_i$  and  $\tau_i$  are given in Table I for each of the transitions [48,49].

Because the primary goal of this work is to determine the

experimental cross section for EIE of the  $1S \rightarrow 1P$  transition, the weighted cross section must be corrected by the procedure enumerated in Eq. (9). As mentioned above, the largest correction to  $\langle \tilde{\sigma} \rangle$  will result from subtraction of the contribution to  $R_{\text{sig}}$  from the  $3P^o \rightarrow 3P$  transition. As we desire to present as pure an experimental quantity as possible, we carried out a separate measurement of the EIE cross section for this transition. This was possible because the  $3p^2 3P$  multiplet radiates at wavelengths near 130 nm. By placing a CaF cutoff filter that rejects radiation below 125 nm in front of the MCP housing, we can uniquely resolve radiation from these levels. The EIE cross section for this transition was measured at four collision energies to verify the overall accuracy of the theoretical calculation. The shape of the cross section is relatively free of resonances; thus a sparse sampling is considered sufficient for the purpose of adjusting  $\langle \tilde{\sigma} \rangle$ . The measured absolute cross section is determined to be  $(3.6 \pm 1.2) \times 10^{-16} \text{ cm}^2$  ( $1.65\sigma$ ) for the two points above threshold. Figure 4 shows the data points for this measurement (solid circles) scaled by the factor  $\xi_i \beta_i = 0.190$ . The lowest theoretical curve is also for this transition, so a direct comparison can be made. There is good agreement between theory and experiment, but the total absolute uncertainty of the measurement is rather large. We can subtract out the contribution to  $\langle \tilde{\sigma} \rangle$  from the  $3s3p^3P^o \rightarrow 3p^2 3P$  transition by scaling the theory for this transition to match the experimental data points. This procedure adds an uncertainty of  $\pm 0.23 \times 10^{-16} \text{ cm}^2$  to the determination of the  $1S \rightarrow 1P$  cross section, computed by applying the factor  $\xi_i \beta_i = 0.190$  to the uncertainty in the  $3P^o \rightarrow 3P$  cross-section measurement (see Table I). This uncertainty is about 3% of the measured average  $1S \rightarrow 1P$  cross section.

To subtract out the contributions to  $\langle \tilde{\sigma} \rangle$  from other transitions, we rely on the theoretical values for the cross sections. Across most of the energy range, the uncertainty in this procedure is expected to be minimal, as the remaining contributors are smaller than the contribution from the  $3P^o \rightarrow 3P$  transition, except at the highest energies. It is difficult to estimate the accuracy of calculations, but even if they are assumed to be accurate to only a factor of 2, the introduced uncertainty is still less than a few percent.

We present the absolute energy-averaged cross section  $\langle \sigma \rangle$  for EIE of the  $1S \rightarrow 1P$  transition in Fig. 5. The data presented here have been corrected to account for the contributions discussed above. As in Fig. 4, the heavy error bars represent the relative uncertainty, and the thin error bars on the 10.8- and 17.2-eV data points represent the total experimental uncertainty (typically 14% for points above threshold).

As mentioned in Sec. II, although the experiment is sensitive to the angular distribution of emitted photons, we make no attempt to measure this distribution. Thus some uncertainty will be introduced when comparing our measurement to theory. We can, however, attempt to place bounds on the possible values of  $Y_\Omega$ , and consequently on the error introduced by setting  $Y_\Omega = 1$ . The most extreme values for the anisotropy arise from assuming that the excitation process results in light polarized parallel to the collision axis ( $P = +1$ ), or perpendicular to it ( $P = -1$ ).  $Y_\Omega$  can then be

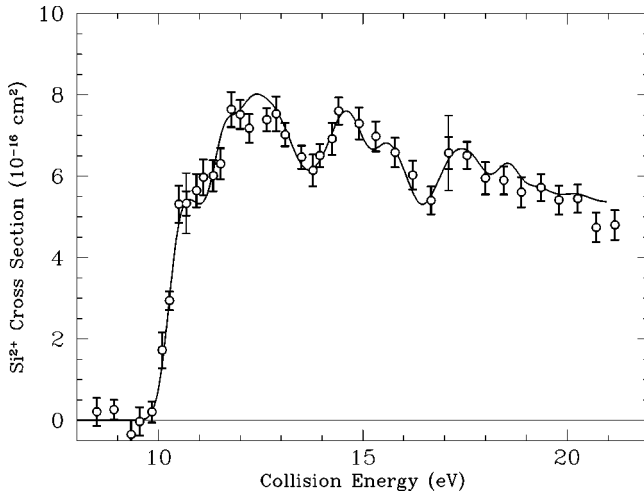


FIG. 5. Absolute energy-averaged EIE cross section for the  $\text{Si}^{2+}(3s^2\ ^1S \rightarrow 3s3p\ ^1P)$  transition. The data presented here have been corrected to account for the contributions from excitation of the metastable state and cascades from higher levels. The heavy error bars on the solid points represent the relative uncertainty, and the thin error bars on the 10.8- and 17.2-eV data points represent the total experimental uncertainty (typically 14% for points above threshold). The solid curve represents the values  $\langle\sigma_j\rangle$  as defined by Eq. (9) for  $^1S \rightarrow ^1P$  excitation. Note that if the anisotropy factor  $Y_\Omega$  differs significantly from 1, it will have the effect of shifting  $\langle\sigma_j\rangle$  in the sense that a positive (negative) polarization will raise (lower) the curve.

calculated from Eq. (3), yielding a value of 1.21 for the first case or 0.90 for the second.

It is unclear what degree of polarization to expect. For neutral Mg (isoelectronic with  $\text{Si}^{2+}$ ), the polarization of  $^1P \rightarrow ^1S$  radiation following electron impact has been observed to approach +1 at threshold, and fall rapidly thereafter (at twice threshold,  $\mathcal{P} = +0.5$ ) [62]. Unfortunately, no polarization measurements or calculations exist for Mg-like ions. In fact, the only polarization investigations for EIE in an isoelectronic system involving  $^1P \rightarrow ^1S$  radiation have been for He-like systems. For neutral He, as in the case of Mg, the threshold value of  $\mathcal{P}$  approaches +1 at threshold [63]; for He-like ions, however, measurements and calculations show the threshold polarization to be significantly less, on the order of  $\mathcal{P} = +0.6$ , across the entire isoelectronic sequence [64,65]. For other ions, EIE experiments that measure the polarization of radiation have generally found that  $\mathcal{P}$  is positive at threshold, and never greater than about +0.25 [66,45]. Based on these observations, it is unlikely that the radiation will be completely polarized in the case of  $\text{Si}^{2+}$  EIE; beyond that, little can be said. It should also be pointed out that in cases where autoionizing resonances contribute a large part of the total cross section, the degree of polarization can vary rapidly as a function of collision energy [67]. We do not include in the experimental uncertainty the error introduced in the comparison to theory by not accounting for the radiation anisotropy.

In order to make the comparisons to theory, we determined the energy spread of the electron beam in the ion rest frame (and the offset potential of the electron gun cathode),

which was then incorporated into Eq. (2) to derive the theoretical energy-averaged cross section. Simple inspection of the raw data strongly suggests that the energy spread must be somewhere between 0.45 and 0.65 eV. The sharpness of the rise of the measured cross section at threshold makes values of the energy spread outside this range unlikely. It can be argued that establishing the energy spread to this level of accuracy is all that is necessary. This is because regardless of what value for the energy spread is chosen within this range, the conclusions drawn from a comparison of the data to theory are essentially unchanged. Nevertheless, it is still necessary to determine the energy spread and scale by quantitative statistical analysis in order to establish the range of uncertainty.

The energy spread and offset potential are statistically evaluated by making two comparisons. First, the data points for the energy-averaged cross section  $\langle\sigma\rangle$  are fit using a  $\chi^2$ -minimization procedure to a Gaussian of variable width convolved with a step function at 10.28 eV, the threshold for  $^1S \rightarrow ^1P$  excitation. Only data 0.5 eV above and below are used in the fit. Points higher than this begin to reflect the expected above-threshold resonance structure, and cannot be compared to a step function. This procedure yields a value for the FWHM energy spread  $\Gamma$  of  $0.51 \pm 0.11$  eV, and an offset potential  $V_o$  of  $2.72 \pm 0.03$  eV. For this fit  $\chi^2_\nu = 1.59$ .

The data are also fit to the convolution of a Gaussian with the theoretical 12CC cross section for the  $^1S \rightarrow ^1P$  transition [48]. The data points for collision energies up to 13.5 eV are used, as points higher than this are not relevant for determining the energy spread. For this case, the best-fit value of  $\Gamma$  is  $0.61 \pm 0.08$  eV, and that of  $V_o$  is  $2.77 \pm 0.02$  eV. For this fit  $\chi^2_\nu = 2.01$ , which is not only a reflection of the uncertainty in the fitting procedure, but also of the discrepancy between the theoretical calculation and the experimental measurement of the cross section.

For both methods, the fitting procedure is iterative, as the data points are derived from  $\langle\tilde{\sigma}\rangle$  by making corrections which in turn require implicit knowledge of the energy spread. The difference in the results of the two methods is an indication of the accuracy of the procedures. The adopted values for the energy spread and offset potential are the average of the above parameters, or  $\Gamma = 0.56 \pm 0.08$  eV and  $V_o = 2.75 \pm 0.02$  eV. The solid line in Figs. 4 and 5 is the energy-averaged 12CC theoretical cross section based on these parameters. Note that the conclusions drawn from the comparison of theory to experiment are insensitive to the choice of energy spread within the range of uncertainty.

#### IV. DISCUSSION

The comparison of theory [48,68] and experiment in Fig. 5 shows excellent agreement for the overall magnitude of the  $^1S \rightarrow ^1P$  excitation cross section. The theoretical cross section lies well within the absolute error bars of the data points. The measurement also generally confirms the shape of the predicted resonance structure. For the resonance grouping between 11 and 13 eV there are some statistically significant variations, although the deviation may be explained by the error in assuming  $Y_\Omega = 1$ . At the highest energies, above 20 eV, there is also a departure from agreement. This most

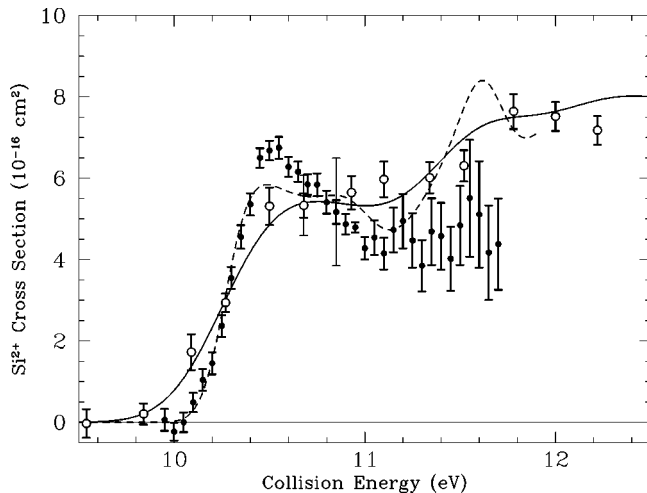


FIG. 6. Absolute energy-averaged EIE cross section for the  $\text{Si}^{2+}(3s^2\ ^1S \rightarrow 3s3p\ ^1P)$  transition, comparing our measurement to the measurement of Wallbank *et al.* (filled circles) [16]. The error bars on their data points represent the relative uncertainty of their measurement, and the thin error bar on the 10.7-eV data point represents the total experimental uncertainty quoted at the 90% confidence level. The dashed line shows the 12CC calculation [48] convolved with a Gaussian representing their experimental energy spread of 0.24-eV FWHM. The portion of Fig. 5 covering the energy range from 9.5 to 12.5 eV is reproduced here, showing our data (open circles) and the 12CC calculation reflecting our energy spread of 0.56 eV (solid line).

likely suggests an overestimation of the cascade corrections from excitation of the  $3s4s\ ^1S$  and  $3s3d\ ^1D$  states, whose excitation thresholds are near 20 eV. Taken together, these states are expected to make a statistically significant contribution to  $\langle \tilde{\sigma} \rangle$  (see Fig. 4). Experience with close-coupling calculations of cascade contributions in other systems suggests that the calculated values of the cross section for these states will be too high unless coupling with yet higher-lying states is included [67,69,70].

Despite the variations, agreement between experiment and theory is remarkable when considered in light of the theoretical complications involved in performing calculations of the resonance structure. Griffin *et al.* [11] showed that the strength of a given resonance is governed by interference between neighboring resonances, and that the interference is extremely sensitive to the exact energies of the resonances. Shifts in resonance positions by less than 1% of the excitation energy can more than double the strength of a given resonance.

Excitation of the  $\text{Si}^{2+}\ ^1S \rightarrow ^1P$  transition for energies near threshold has been measured by Wallbank *et al.* [16] using the electron-energy-loss method. Their results are shown as the filled circles in Fig. 6. The error bars on the data points represent the relative uncertainty of their measurement, and the large error bar on the data point at 10.7 eV represents the total experimental uncertainty quoted at the 90% confidence level. The dashed line shows the 12CC calculation convolved with a Gaussian representing their reported energy spread of 0.24-eV FWHM. The data of Wallbank *et al.* show a rapid growth in statistical uncertainty for energies above

11.1 eV. This is a consequence of their inability to detect electrons which backscatter in the laboratory frame. The signal rates for collision energies above 10.6 eV are all corrected for the loss of backscattered electrons. Above 11.7 eV the backscatter correction grows to more than a factor of 2; thus no more measurements were made above the point. The correction factors were determined from a trajectory modeling program and theoretical calculations of the differential cross section as a function of the electron scattering angle. They also detected a persistent signal below threshold equivalent to a cross section of  $(1.316 \pm 0.036) \times 10^{-16}\ \text{cm}^2$ , which they subtract from the cross sections shown in Fig. 6. They attribute part of this signal to the collection of inelastically scattered electrons from the  $3s3p\ ^3P^o \rightarrow 3p^2\ ^3P$  transition. The assumption that this background may be subtracted is not included in their total uncertainty.

For comparison to our measurement, the portion of Fig. 5 covering the energy range from 9.5 to 12.5 eV is reproduced in Fig. 6. A direct comparison between the experiments is not possible because of the significant difference in energy spread. We can, however, comment on how each experiment compares with theory. The data of Wallbank *et al.* show a somewhat higher cross section than theory at threshold, while theory is significantly higher at the upper end of their energy coverage, growing to about 50% above their measured cross section. Our data, which have a significantly smaller total uncertainty, are in much closer agreement with theory across this energy range.

It is worthwhile to place our measurement in the context of resonance-resolving measurements of other systems. Absolute measurements of the resonance structure have recently been performed for the multiply-charged ions  $\text{Kr}^{6+}$  [14] and  $\text{Ar}^{6+}$  [15]. In both cases, comparison to theory has been mixed. For  $\text{Kr}^{6+}(4s^2\ ^1S \rightarrow 4s4p\ ^3P^o)$ , theory could only be brought into convergence with experiment by arbitrarily shifting the energy position of key resonances. For this system, where the cross section is totally dominated by resonance structure, shifts in resonance position of more than 0.5 eV would not be surprising, and resonance strengths can vary by more than 30% as a result. In  $\text{Ar}^{6+}$ , which is isoelectronic with  $\text{Si}^{2+}$ , EIE has been measured for two transitions: for the  $3s^2\ ^1S \rightarrow 3s3p\ ^1P$  dipole-allowed excitation and the  $3s^2\ ^1S \rightarrow 3s3p\ ^3P^o$  intercombination excitation. Good agreement was found for the  $^1S \rightarrow ^1P$  excitation, as in our case; however, for the  $^1S \rightarrow ^3P^o$  excitation the resonance at threshold was measured to have twice its predicted strength.

The measurement presented here demonstrates that, at least for this case, atomic scattering theory is capable of predicting accurate EIE cross sections when resonance contributions are significant. Nevertheless, so few systems have been studied, and with such mixed results, that a good deal of work remains to be done.

## V. SUMMARY

We have determined the absolute cross section for electron-impact excitation (EIE) of  $\text{Si}^{2+}(3s^2\ ^1S \rightarrow 3s3p\ ^1P)$  for energies in the range 8.5 to 21.5 eV. The population of the  $\text{Si}^{2+}(3s3p\ ^3P^o)$  metastable state in the incident ion

beam was determined to be  $0.210 \pm 0.018$ . The data were corrected for contributions to the signal from excitation of the metastable state, and at higher energies, for excitation of the ground state to levels above the  $3s3p^1P$  level. The experimental  $0.56 \pm 0.08$ -eV energy spread allowed us to detect complex resonance structure throughout the studied energy range. At the reported 14% uncertainty level (90% confidence limit), the measured structure and absolute scale of the cross section are in good agreement with 12-state close-coupling  $R$ -matrix calculations [48,68].

## ACKNOWLEDGMENTS

The authors thank J. H. Chappell, A. Daw, D. Griffin, and W. H. Parkinson for assistance and stimulating discussions. The authors also thank D. Hoey, C. B. Hughes, and F. P. Rivera for their technical assistance. This work was supported by NASA Supporting Research and Technology Program in Solar Physics Grants No. NAGW-1687 and No. NAG5-5059, the Smithsonian Astrophysical Observatory, and by a NASA Training Grant No. NGT-51081 to D. B. R.

- 
- [1] J. T. Mariska, *The Solar Transition Region* (Cambridge University Press, Cambridge, England, 1992).
- [2] D. E. Osterbrock, *Astrophysics of Gaseous Nebulae and Active Galactic Nuclei* (University Science, Mill Valley, CA, 1989).
- [3] T. R. Gull, in *Insights in Astrophysics. Eight years of UV Astronomy with IUE. Proceedings of an International Symposium (ESA SP-263)* (ESA, Noordwijk, The Netherlands, 1986), p. 653.
- [4] D. R. Garnett *et al.*, *Astrophys. J. Lett.* **449**, L77 (1995).
- [5] *The SOHO Mission*, edited by B. Fleck, V. Domingo, and A. I. Poland (Kluwer, Dordrecht, 1995).
- [6] M. C. Weisskopf and S. L. O'Dell, *Soc. Photo-Opt. Instrum. Eng.* **3113**, 2 (1997).
- [7] J. L. Kohl *et al.*, *Sol. Phys.* **162**, 313 (1995).
- [8] K. Wilhelm *et al.*, *Appl. Opt.* **36**, 6416 (1997).
- [9] G. H. Dunn *et al.*, *Nucl. Instrum. Methods Phys. Res. B* **98**, 107 (1995).
- [10] R. J. W. Henry, *Rep. Prog. Phys.* **56**, 327 (1993).
- [11] D. C. Griffin *et al.*, *Phys. Rev. Lett.* **72**, 3491 (1994).
- [12] W. Rogers, J. O. Olsen, and G. H. Dunn, *Phys. Rev. A* **18**, 1353 (1978).
- [13] S. Chantrenne, P. Beiersdorfer, R. Cauble, and M. B. Schneider, *Phys. Rev. Lett.* **69**, 265 (1992).
- [14] M. E. Bannister, X. Q. Guo, T. M. Kojima, and G. H. Dunn, *Phys. Rev. Lett.* **72**, 3336 (1994).
- [15] Y.-S. Chung, N. Djurić, B. Wallbank, and G. H. Dunn, *Phys. Rev. A* **55**, 2044 (1997).
- [16] B. Wallbank *et al.*, *Phys. Rev. A* **56**, 3714 (1997).
- [17] T. W. Gorczyca, F. Robicheaux, M. S. Pindzola, and N. R. Badnell, *Phys. Rev. A* **52**, 3852 (1995).
- [18] T. W. Gorczyca, M. S. Pindzola, N. R. Badnell, and D. Griffin, *Phys. Rev. A* **51**, 488 (1995).
- [19] A. R. Young, Ph.D. thesis, Harvard University, 1990.
- [20] D. W. Savin *et al.*, *Phys. Rev. A* **51**, 2162 (1995).
- [21] D. W. Savin *et al.*, *Phys. Rev. A* **53**, 280 (1996).
- [22] A. R. Young *et al.*, *Phys. Rev. A* **49**, 357 (1994).
- [23] H. E. Mason and B. C. Monsignori-Fossi, *Astron. Astrophys. Rev.* **6**, 123 (1994).
- [24] J. L. Linsky *et al.*, *Astrophys. J.* **442**, 381 (1995).
- [25] A. Ciaravella *et al.* (unpublished).
- [26] P. L. Dufton, A. Hibbert, A. E. Kingston, and G. A. Doscher, *Astrophys. J.* **274**, 420 (1983).
- [27] F. P. Keenan, J. W. Cook, P. L. Dufton, and A. E. Kingston, *Astrophys. J.* **340**, 1135 (1989).
- [28] F. P. Keenan, P. Dufton, and A. E. Kingston, *Sol. Phys.* **123**, 33 (1989).
- [29] P. O. Taylor *et al.*, *Phys. Rev. Lett.* **39**, 1256 (1977).
- [30] G. P. Lafyatis and J. L. Kohl, *Phys. Rev. A* **36**, 59 (1987).
- [31] D. Gregory, G. Dunn, R. A. Phaneuf, and D. H. Crandall, *Phys. Rev. A* **20**, 410 (1979).
- [32] D. B. Reisenfeld, L. D. Gardner, P. H. Janzen, and J. L. Kohl (unpublished).
- [33] G. P. Lafyatis, J. L. Kohl, and L. D. Gardner, *Rev. Sci. Instrum.* **58**, 383 (1987).
- [34] L. D. Gardner *et al.*, *Rev. Sci. Instrum.* **57**, 2254 (1986).
- [35] G. W. Fraser, *Nucl. Instrum. Methods Phys. Res. A* **291**, 595 (1990).
- [36] J. A. Schecker, M. M. Schauer, K. Holzscheiter, and M. H. Holzscheiter, *Nucl. Instrum. Methods Phys. Res. A* **320**, 556 (1992).
- [37] G. Melin *et al.*, *Rev. Sci. Instrum.* **65**, 1051 (1994).
- [38] P. Sortais, *Rev. Sci. Instrum.* **67**, 867 (1996).
- [39] Y. Jongen and C. M. Lyneis, in *The Physics and Technology of Ion Sources*, edited by I. G. Brown (Wiley, New York, 1989), p. 207.
- [40] M. Liehr, R. Trassl, M. Schlapp, and E. Salzborn, *Rev. Sci. Instrum.* **63**, 2541 (1992).
- [41] O. H. W. Siegmund *et al.*, *Appl. Opt.* **26**, 3607 (1987).
- [42] G. W. Fraser, *X-ray Detectors in Astronomy* (Cambridge University Press, Cambridge, 1989), Chap. 3.
- [43] C. I. Coleman, *Rev. Sci. Instrum.* **53**, 735 (1982).
- [44] I. C. Percival and M. J. Seaton, *Philos. Trans. R. Soc. London* **251**, 113 (1958).
- [45] P. O. Taylor and G. H. Dunn, *Phys. Rev. A* **8**, 2304 (1973).
- [46] U. Fano and J. H. Macek, *Rev. Mod. Phys.* **45**, 553 (1973).
- [47] D. B. Reisenfeld, Ph.D. thesis, Harvard University, 1998.
- [48] D. C. Griffin, M. S. Pindzola, and N. R. Badnell, *Phys. Rev. A* **47**, 2871 (1993).
- [49] K. L. Baluja and A. Hibbert, *J. Phys. B* **13**, L327 (1980).
- [50] D. R. Lide, *CRC Handbook of Chemistry and Physics* (CRC Press, Boca Raton, FL, 1994).
- [51] C. Liao, J. Smith, A. Chutjian, and D. Hitz, *Phys. Scr.* **T73**, 382 (1997).
- [52] H. B. Gilbody, in *Low-energy Ion Beams, 1977*, edited by K. G. Stephens, I. H. Wilson, and J. L. Moruzzi, IOP Conf. Proc. No. 38 (Institute of Physics and Physical Society, London, 1978), Chap. 4, p. 56.
- [53] H. S. Kwong, B. C. Johnson, P. L. Smith, and W. H. Parkinson, *Phys. Rev. A* **27**, 3040 (1983).
- [54] P. Jonsson and C. F. Fischer, *J. Phys. B* **30**, 5861 (1997).
- [55] C. D. Lin, C. Laughlin, and G. A. Victor, *Astrophys. J.* **220**, 734 (1978).

- [56] M. Zuo *et al.*, *Astrophys. J.* **440**, 421 (1995).
- [57] B. R. Turner, J. A. Rutherford, and D. M. J. Compton, *J. Chem. Phys.* **48**, 1602 (1968).
- [58] G. P. Lafyatis, Ph.D. thesis, Harvard University, 1982.
- [59] G. H. Dunn, in *Atomic Physics*, edited by B. Bederson, V. W. Cohen, and F. M. J. Pichanick (Plenum Press, New York, 1969).
- [60] K. T. Dolder and B. Peart, *Rep. Prog. Phys.* **39**, 693 (1976).
- [61] *Atomic Energy Levels*, edited by C. E. Moore, Natl. Bur. Stand. U.S. Circ. No. 35 (U.S. GPO, Washington, DC, 1971).
- [62] M. B. Shapochkin and E. V. Petrov, *Phys. Scr.* **52**, 52 (1995).
- [63] C. Norén, J. W. McConkey, P. Hammond, and K. Bartschat, *Phys. Rev. A* **53**, 1559 (1996).
- [64] K. J. Reed and M. H. Chen, *Phys. Rev. A* **48**, 3644 (1993).
- [65] P. Beiersdorfer *et al.*, *Phys. Rev. A* **53**, 3974 (1996).
- [66] D. H. Crandall, R. A. Phaneuf, and G. H. Dunn, *Phys. Rev. A* **11**, 1223 (1975).
- [67] J. Mitroy, D. C. Griffin, D. W. Norcross, and M. S. Pindzola, *Phys. Rev. A* **38**, 3339 (1988).
- [68] K. L. Baluja, P. J. Burke, and A. E. Kingston, *J. Phys. B* **13**, L543 (1980).
- [69] J. Mitroy and D. Norcross, *Phys. Rev. A* **37**, 3755 (1988).
- [70] J. Mitroy and D. W. Norcross, *Phys. Rev. A* **39**, 537 (1989).